



Universidad Autónoma
de Madrid

Biblos-e Archivo
Repositorio Institucional UAM

Repositorio Institucional de la Universidad Autónoma de Madrid

<https://repositorio.uam.es>

Esta es la **versión de autor** del artículo publicado en:
This is an **author produced version** of a paper published in:

Journal of Alloys and Compounds 910 (2022): 164905

DOI: <https://doi.org/10.1016/j.jallcom.2022.164905>

Copyright: © 2022 Elsevier B.V. All rights reserved.

This manuscript version is made available under the CC-BY-NC-ND 4.0
licence <http://creativecommons.org/licenses/by-nc-nd/4.0/>

El acceso a la versión del editor puede requerir la suscripción del recurso
Access to the published version may require subscription

Spinel to disorder rock-salt structural transition on (111) nickel ferrite thin films tailored by Ni content

P. Prieto¹, A. Serrano², R. E. Rojas-Hernández³, S. Gorgojo¹, José E. Prieto⁴, L. Soriano¹

¹ *Departamento de Física Aplicada M-12 and Instituto Nicolas Cabrera, Universidad Autónoma de Madrid, E-28049 Madrid, Spain*

² *Departamento de Electrocerámica, Instituto de Cerámica y Vidrio (ICV), CSIC, 28049 Madrid, Spain*

³ *Department of Materials Engineering, Tallinn University of Technology, Ehitajate 5, 19180 Tallin, Estonia*

⁴ *Instituto de Química Física “Rocasolano” (IQFR), CSIC, C/ Serrano 119, E-28006 Madrid, Spain*

(111)-oriented $\text{Ni}_x\text{Fe}_{3-x}\text{O}_y$ thin films with varying Ni content ($0.7 \leq x \leq 1.7$) have been grown on c-plane (0001) $\alpha\text{-Al}_2\text{O}_3$ substrates by ion beam sputtering. Epitaxial $\text{Ni}_x\text{Fe}_{3-x}\text{O}_y$ thin films with spinel structure are obtained for $x \leq 1$. For nickel content exceeding the value of the stoichiometric phase, i.e. NiFe_2O_4 , a transition from an ordered spinel to a disordered rock-salt phase is identified, being the dominant one when $x = 1.7$. This result is confirmed by X-ray diffraction, Rutherford backscattering spectroscopy in channeling configuration, Raman spectroscopy, X-ray absorption near-edge structure (XANES) and extended X-ray absorption fine structure (EXAFS). We also report the first Raman spectra in $\text{Ni}_x\text{Fe}_{3-x}\text{O}_y$ with mainly rock-salt structure. The evolution of the electrical and optical properties of the (111) $\text{Ni}_x\text{Fe}_{3-x}\text{O}_y$ films as Ni content increases, supports the structural change. The electrical resistivity increases up to $10^3 \text{ ohm}\cdot\text{cm}$, the direct and indirect band gaps also increase and only one direct band gap, instead of the two characteristic of the spinel structure, is present in the $\text{Ni}_x\text{Fe}_{3-x}\text{O}_y$ film with $x=1.7$.

Corresponding author:

e-mail: pilar.prieto@uam.es; fax: +34 91 4973969; tel: +34 91 4975265

KEYWORDS: Nickel ferrite, spinel-to-rock-salt transition, XANES and EXAFS, RBS_channeling, physical properties

Introduction

Nickel ferrite, NiFe_2O_4 , is one the most interesting spinel ferrites due to properties such as its relative high Curie temperature, i.e. 865 K, high saturation magnetization [1], large bandgap of 1.65 eV [2] and moderate magnetostriction, giving potential applications on sensors and high frequency microwave applications as phase shifter [3]. NiFe_2O_4 shows also different barrier heights for spin-up and spin-down electrons, which can produce highly spin-polarized currents and large magnetoresistance [4]. In fact, in the field of spintronics, applications as electrodes or tunnel barriers in spin-filter devices [6] are being developed due to its controllable transport properties. In this case high crystalline quality thin films are needed since the spin-tunneling probability decreases exponentially with the tunneling barrier thickness.

NiFe_2O_4 has an inverse spinel ($Fd\bar{3}m$) structure with half of the Fe^{3+} cations occupying tetrahedral A sites, while the remaining Fe^{3+} and Ni^{2+} cations are distributed on the octahedral B sites [5]. A short-range 1:1 ordering of Fe^{3+} and Ni^{2+} at the B sites of the inverse spinel structure has been determined [6]. The magnetic structure of NiFe_2O_4 is well explained by the Néel model of ferrimagnetism, where a strong super-exchange interaction between the nearest neighbor tetrahedral and octahedral cations via oxygen results in anti-parallel alignment of the local magnetic moment of the cations at these sites. In addition, there is a double-exchange interaction between Fe^{3+} and Ni^{2+} cations at octahedral sites with ferromagnetic coupling.

Currently, there are a considerable number of deposition technique available for $\text{Ni}_x\text{Fe}_{3-x}\text{O}_y$, NFO, thin films such as pulsed laser deposition (PLD) [7, 8, 9], atomic layer deposition (ALD) [10], chemical vapor deposition (CVD) [11], molecular beam epitaxy (MBE) [12], reactive sputtering and co-sputtering [13, 14, 15] and chemical methods such as sol-gel processes [16]. In all of them, the most explored phase in both, nanostructure and thin film forms, is the stoichiometric one, i.e. NiFe_2O_4 . Several works have been focused on thin films to integrate them on heteroepitaxial devices. For example, by studying the growth and properties of (100) NiFe_2O_4 thin films on single crystal substrates such as (100) MgAl_2O_4 , in which the lattice mismatch is as small as 1.3% [13, 17]. Other (100) (110) and (111) SrTiO_3 oriented substrates [2, 8, 18] have been also explored. Even (111)-oriented NiFe_2O_4 films, but polycrystalline, have been obtained by growing on c-sapphire substrates [19, 20].

The deviation found on the properties of NiFe_2O_4 thin films from those of single NiFe_2O_4 crystals can be related to lattice disorder due to the non-equilibrium growth conditions and structural differences originated by the mismatch between the lattice parameters of the film and substrate. In general, the various degrees of freedom in complex oxides allow tailoring their thin film properties by choosing appropriate growth conditions. Oxygen partial pressure [8, 9], growth temperature and thickness are the most studied parameters to tailor the physical properties of NFO thin films. In particular, it has been established that the presence of cation/oxygen vacancies is crucial for the magnetic and transport properties of the NFO films [9]. Another parameter that has an important effect in the physical properties of NFO films, but has been less explored, is the relative concentration of Fe and Ni cations. In fact, scarce studies have been carried out on non-stoichiometric NFO films, i.e. $\text{Ni}_x\text{Fe}_{3-x}\text{O}_4$, and most of them are concentrated on polycrystalline films [21, 22] and (100)-oriented

1
2
3
4 films [11, 22, 23]. On the one hand, in the low Ni content range, i.e. $x < 1$ in $\text{Ni}_x\text{Fe}_{3-x}\text{O}_4$,
5 Pachauri *et al.* [11] concentrate their work on the study of (100) $\text{Ni}_x\text{Fe}_{3-x}\text{O}_4$ thin
6 films grown by CVD technique on cubic (100) MgAl_2O_4 substrates, while C. Kim *et*
7 *al.* [22] focus their work on the growth of the films by co-sputtering technique on
8 (100) MgO substrates. On the other hand, in the high Ni content range (i.e. $x > 1$ in
9 $\text{Ni}_x\text{Fe}_{3-x}\text{O}_4$), reactive MBE has been used to grow $\text{Ni}_x\text{Fe}_{3-x}\text{O}_4$ on (100) MgO [23].
10 However, the (111)-oriented non-stoichiometric nickel ferrite thin films have only been
11 studied in the low Ni content range ($x < 1$) by Bratvold *et al.* [10] and focusing
12 mainly the research on the growth mechanism. Therefore, the physical properties of
13 (111)-oriented NFO films remain unstudied, which occur in both the low ($x < 1$) and high
14 ($x > 1$) Ni compositional range.

15
16
17
18
19 In this paper we report the growth of (111)-oriented $\text{Ni}_x\text{Fe}_{3-x}\text{O}_y$ thin films by ion beam
20 sputtering (IBS) in a wide compositional range ($0.7 \leq x \leq 1.7$). We focus our study on the
21 transformation from spinel to rock-salt structure accompanied by a loss of crystalline order
22 when x exceeds the stoichiometric value, i.e. $x > 1$, result that is confirmed in terms of
23 cation environment changes at short range. The electrical and optical properties of the films
24 are in agreement with the structural change and the loss of crystallinity observed.

25 26 27 28 29 30 31 32 33 34 35 36 37 38 39 40 41 42 43 44 45 46 47 48 49 50 51 52 53 54 55 56 57 58 59 60 61 62 63 64 65

Experimental

NFO thin films were deposited on (0001) $\alpha\text{-Al}_2\text{O}_3$ substrates by IBS using Ar^+ ions
from a 3 cm Kaufmann-type ion source in a controlled atmosphere of O and Ar from
metallic mixed Ni-Fe targets (99.99% purity) in a vacuum chamber under a base pressure
of 2×10^{-5} Pa. This technique offers an independent control of both the ion energy and ion
current density allowing the arrival of high energy atoms at the substrate. Therefore, a high
surface diffusion and, in general, a high packing density of the deposited films is achieved.
During deposition the pressure was maintained at 3.4×10^{-2} Pa and the substrates were
rotated at 2 rpm to increase the homogeneity of the deposit. Since we have focused our
work in the effect of the Ni content on the ferrite, by modifying the Ni-Fe target, we have
used the same deposition parameters for all the studied films. The substrate temperature
during deposition was maintained to 470 °C, the oxygen partial pressure to 4.6×10^{-3} Pa,
the sputtering current density, J_{sp} , was fixed to 1.64 mA/cm² and the energy of the sputter
 Ar^+ ions, E_{sp} , was fixed to 650 eV.

The elemental composition of the NFO films was determined by using a Hitachi
S-3000N scanning electron microscope complemented with an energy dispersive
spectrometer operating at 5 kV. The crystal structure and texture of the different films
were analyzed by X-ray diffraction (XRD) in a $\Theta/2\Theta$ configuration using a PANanalytical
X'Pert MPD system and Cu-K α radiation.

In-depth composition and thickness of the different layers were determined by
Rutherford backscattering spectroscopy (RBS) in a 5 MV tandem accelerator using
 $^4\text{He}^+$ at 1.8 MeV [24]. The distribution and in-depth quantification of the various
elements was determined with the SIMNRA simulation software package [25]. The ion
fluence used was 20 μC . A silicon barrier detector, at a scattering angle of 170.5°, was
used to measure the backscattering yield, while a three-axis goniometer was employed

to control the crystal position. The measurements were carried out in both random and channeling configurations. If the film grows epitaxial and the direction of the incident 4He^+ particles is aligned with a high-symmetry direction of the crystal lattice, most of incoming ions pass through the channel provided by the empty space available within the crystal lattice and penetrate deep into the material. The resultant decrease of the scattering yield is a measure of the epitaxial quality of the films.

Raman experiments were carried out using a Witec alpha-300RA instrument with a Nd:YAG laser of 532 nm. Raman spectra were collected by fixing the laser excitation power at 3 mW, using a 1800 g/mm grating and an objective with a numerical aperture of 0.95. An average Raman spectrum for each sample was obtained averaging 20 spectra with 5 s of integration time. Several regions of films were measured in order to analyze the film homogeneity. Additionally, Raman spectra of the stoichiometric film were measured by varying the light polarization in xx, xy, yx and yy configuration. The first and second letter in the configuration notations denotes the polarization of the incident and scattered light, respectively. Raman results were analyzed by using Witec Project Plus Software.

X-ray absorption spectroscopy (XAS) was performed on the films at the CLÆSS-BL22 beamline of the ALBA synchrotron facility in Cerdanyola del Vallès (Spain) [26]. Both X-ray absorption near-edge structure (XANES) and extended X-ray absorption fine structure (EXAFS) experiments were achieved at room temperature in fluorescence mode at the Fe (7112 eV) and Ni (8333 eV) K-edges. The monochromator used in the experiments was a double Si crystal oriented in the (311) direction. Metal foils were measured and used to calibrate the energy. NiO, FeO, $\alpha\text{-Fe}_2\text{O}_3$ and Fe_3O_4 references in powder form were mixed with cellulose and pressed into pellets to be measured in transmission configuration.

Both the electrical and the optical properties of samples were carried out. The electrical characterization of films was performed by the four probe method using a Jandel probe between room temperature and 200°C, evaluating the electrical resistivity. Transmittance and reflectance optical spectra were taken by means of an UV-VIS Jasco V-560 double-beam spectrophotometer equipped with an integrated sphere to avoid errors due to diffuse light scattering of the samples. Tauc's plots were used to determine the optical bandgaps.

Result and Discussion

Fig. 1a shows the energy dispersive spectroscopy (EDS) spectra of the $\text{Ni}_x\text{Fe}_{3-x}\text{O}_y$ thin films varying the Fe/Ni content, i.e. x . The films show a high uniformity degree. The reported EDS spectra are the average of three EDS spectra obtained in different regions. The presence of O, Fe and Ni as well as the different Fe/Ni ratios can be observed in the figure. The elemental chemical composition evolution was also confirmed by other quantitative technique as RBS. Fig. 1b shows the random RBS spectrum obtained for sample $\text{Ni}_{1.0}\text{Fe}_{2.0}\text{O}_y$ including the elemental in-depth concentrations. The denotation of the films, the cationic composition x obtained by the two compositional techniques, its average value, as well as the thicknesses of the film calculated by SIMNRA simulations have been included in Table 1. The RBS and EDS techniques are scarcely sensitive to determine the oxygen concentration. Specifically, in the case of RBS spectra the oxygen signal from the film overlaps with the Al and O signal from the Al_2O_3 substrate leading to errors in the O concentration of up to 10%. Therefore, the discussion will be done using the $\text{Ni}_x\text{Fe}_{3-x}\text{O}_y$ notation. Fig. 1a also includes the denotation of the nickel ferrite thin films based on the average compositions.

The structural properties of $\text{Ni}_x\text{Fe}_{3-x}\text{O}_y$ thin films were investigated by XRD in θ -2 θ configurations. Fig.2a shows the XRD scans for $\text{Ni}_x\text{Fe}_{3-x}\text{O}_y$ thin films with $x = 1.0$ and $x = 1.2$. Pronounced (111), (222) and (333) diffraction peaks, characteristic of the spinel structure, can be observed with no additional peaks observable except to that corresponding to the (0001) $\alpha\text{-Al}_2\text{O}_3$ diffraction peak from the substrate indicating that the films grow epitaxially without any parasitic phase. In fact, the in-plane lattice parameter $a_{\text{NFO}} \sim \sqrt{3}a_{\text{Al}_2\text{O}_3}$ and the expected growth of NFO on c-cut of Al_2O_3 substrates is (111)-oriented and rotated 30° with respect to the basis of (0001) Al_2O_3 plane [10]. Specifically, Fig. 2a presents observable differences in the relative intensity between (111), (222) and (333) diffraction peaks of samples $\text{Ni}_{1.0}\text{Fe}_{2.0}\text{O}_y$ and $\text{Ni}_{1.2}\text{Fe}_{1.8}\text{O}_y$. Thus, to compare the diffraction pattern of the different $\text{Ni}_x\text{Fe}_{3-x}\text{O}_y$ films we have focused on the relative intensity between the NFO (XXX) diffraction peaks. The relationship between the intensity changes of the (XXX) diffraction peaks and the film composition is observed in Fig. 2b, in which the relative intensity of (111) and (333) diffraction peaks with respect to the (222) peak is plotted as a function of Ni content, i.e. x in $\text{Ni}_x\text{Fe}_{3-x}\text{O}_y$. It can be identified a maximum value for $x = 1.0$ while for $x = 1.7$ the (111) and (333) peaks completely disappear. The absence of the (111) and (333) peak in $\text{Ni}_{1.7}\text{Fe}_{1.3}\text{O}_y$ thin film could be an indication that a structural change has taken place.

For rock-salt structures, the presence of the (111) diffraction peak is expected at similar 2θ angles as the (222) diffraction peak of spinel structures. References of FeO [27] and NiO [28] give (111) diffraction peaks at 36.0° and 37.2° , respectively, while the (222) diffraction peak of NiFe_2O_4 of the spinel structure appears at 37.2° [29]. Therefore, Fig. 2b could show a structural phase transition, relate to the spinel to rock-salt structural transition and followed by the intensity ratio $I(\text{XXX})/I(222)$ as a function of x in $\text{Ni}_x\text{Fe}_{3-x}\text{O}_y$ films, reaching a zero value when $x = 1.7$. This could be an indication of the presence of a rock-salt structure instead of the spinel one observed in the stoichiometric phase, i.e. $x=1$, in which these ratios show the maximum values. At this point, it should be mentioned that to

the best of our knowledge a rock-salt structure has not been reported before for nickel ferrite thin films, however it has been reported for other spinels as NiCo_2O_4 [30].

A detail of the (111) rock-salt or (222) spinel 2 θ diffraction region is shown in Fig. 2c. For samples with Ni content in the range $0.7 \leq x \leq 1.2$, it can be observed a shift to higher angles as Ni content increases, i.e. a shift to lower lattice constant. For $x = 1.7$ the (111) diffraction peak falls to similar values as the (222) spinel peak of $\text{Ni}_{0.7}\text{Fe}_{2.3}\text{O}_y$ thin film showing a greater width. Fig. 2d shows the evolution of the out-plane lattice parameter with the Ni content, i.e. x in $\text{Ni}_x\text{Fe}_{3-x}\text{O}_y$. We have plotted the values obtained from the peaks corresponding to (222) diffraction plane of spinel phase or (111) diffraction plane of the rock-salt phase. For comparative purposes, the lattice parameter of the bulk spinel NiFe_2O_4 phase is included. The observed decrease of the lattice parameter value is an indication of a compressive strain reduction with increasing Ni content until $x=1.2$. A similar behavior, in terms of vertical layer distance, has been observed by Rodewald *et al.* for ultrathin $\text{Ni}_x\text{Fe}_{3-x}\text{O}_4$ spinel films on (001) MgO [23]. However, when x reaches its highest value, i.e. $x=1.7$, the lattice parameter does not follow this evolution with x , increasing again, thus supporting that a structural change could be taking place. In addition, the crystal size has been obtained by using the Scherrer's formula and it is plotted in Fig. 2e as a function of Ni content. The decrease of crystallite size from 120 to 56 nm obtained as x increases indicates that the proposed structural transition from spinel to rock-salt phase in (111) NFO thin films is accompanied by a loss of crystallinity.

RBS technique is generally used to determine the chemical composition, thickness and in-depth atomic distribution of the different elements present in the film, however it can also be used to explore the epitaxial nature of thin films. Fig. 3a and 3b show the random and channeling spectra of $\text{Ni}_{1.0}\text{Fe}_{2.0}\text{O}_y$ and $\text{Ni}_{1.2}\text{Fe}_{1.8}\text{O}_y$ thin films, respectively. Comparing the curves of both samples, it is clear that the yield decreases in the channeling spectra when the (111) film is aligned with the (0001) Al_2O_3 substrate, confirming the epitaxial character of the films. In addition, the ratio between yields of channeling and random spectra can be used as an indicator of the epitaxial or crystalline degree of the deposited film. The lineshape of the RBS/channeling spectrum also indicates the in-depth distribution of the density of defects or structural disorders. The RBS/channeling spectrum of $\text{Ni}_{1.0}\text{Fe}_{2.0}\text{O}_y$ film shows a yield ratio value at the interface of 46%, significantly higher than those to the film surface with a minimum yield ratio before the peak surface, χ_{\min} , of 12%, indicating higher disorder at the interface due to lattice mismatch. In the case of the $\text{Ni}_{1.2}\text{Fe}_{1.8}\text{O}_y$ thin film, both values are significantly higher than the ones of stoichiometric film, i.e. $\chi_{\text{interface}} = 65\%$ and $\chi_{\min} = 52\%$, indicating a loss of crystalline order as the Ni content increases. In fact, the film with the highest Ni content thin film, i.e. $\text{Ni}_{1.7}\text{Fe}_{1.3}\text{O}_y$, does not show any decrease of the yield in any direction. To clarify, Fig.3c shows the $\chi_{\text{interface}}$ and χ_{\min} as a function of Ni content. For $x \leq 1$, the (111) NFO films show similar values of both yield ratios, however as the Ni content exceeds the stoichiometric value both $\chi_{\text{interface}}$ and χ_{\min} values increase with the Ni content. This behavior indicates the loss of crystalline degree as the structural transition from spinel to rock-salt occurs, as observed by XRD, identifying a fully disorder structure for $x = 1.7$.

Raman spectroscopy is also a suitable technique to determine not only structural changes in spinel structures but also the ordering of the cations at tetrahedral and octahedral sites. In

spinel $Fd\bar{3}m$ structure there are five Raman active modes $A_{1g} + E_g + 3F_{2g}$ [6]. Fig.4a shows the Raman spectra of the NFO films in xx scattering configuration of the $Ni_xFe_{3-x}O_y$ thin films varying the Ni content. In the case of stoichiometric film, i.e. $x=1$, it can be distinguished seven Raman band at 695, 655, 570, 481, 328, 203 and 185 cm^{-1} . Although the presence of more bands cannot be resolved, it should be mentioned that the bands at 481 and 328 cm^{-1} are clearly asymmetrical, compatible with the shoulder-like structure that can be identified in the bands at 695 and 203 cm^{-1} . To explain the presence of more active bands than the expected ones, we have to start first with the sharper five Raman active bands: $A_{1g} + E_g + 3F_{2g}$ observed in Fe_3O_4 spinel, which seem to show a shoulder-like structure in the case of close to stoichiometric $NiFe_2O_4$ films due to the substitution of Fe^{2+} ions by Ni^{2+} ions, with different ionic radii. This substitution is the cause of a distribution of the Fe/Ni-O distances, resulting in a double-like structure in the spectrum of NFO spinel structure. In this model, probably one represents the unit cell with all Fe ions and the other one with mixed Fe and Ni ions [31]. In fact, the most intense Raman peak at 695 cm^{-1} corresponds to symmetrical stretching vibration of the oxygen atoms at tetrahedral sites, while the shoulder at 655 cm^{-1} has been assigned to a partial Ni for Fe substitution of tetragonal sites [6]. Larger Ni-O bonds respect to Fe-O bonds change the energy of the stretching vibrations. The other main bands at 570, 481, 328 and 203 cm^{-1} are due to the symmetric and antisymmetric bending of oxygen atom in M-O bonds at octahedral sites and the shoulder-like structure can again be associates with energy changes of the bending vibrations due to partial Ni for Fe substitution.

Small differences in Raman bands for $Ni_xFe_{3-x}O_y$ with $x \leq 1.2$ can be observed on Fig. 4a. Related to the intensity of the A_{1g} band, it can be observed that the intensity of the bands at ≈ 481 , 328 and 203 cm^{-1} decreases while the intensity of the 570 cm^{-1} band increases as the Ni content increases. This can be attributed to the different distribution of the Fe/Ni-O distances depending on the Ni/Fe ratio. However, in the NFO film with the highest Ni content, i.e. $x = 1.7$, the characteristics of Raman spectrum completely change showing only a main band at 550 cm^{-1} and another of lower intensity about 680 cm^{-1} . The presence of these two Raman modes is consistent by considering the rock-salt structure obtained at the highest Ni content film ($Ni_{1.7}Fe_{1.3}O_y$). In general, the rock-salt structure exhibits weak Raman scattering and the first-order phonon modes are forbidden [32]. However, an enhancement of the first-order phonon scattering can occur because of the presence of vacancies or structural defects in the samples. According to the literature, the asymmetric band at 550 cm^{-1} corresponds to the longitudinal optical (LO) Raman scattering of Ni—O vibrations while the mode about 680 cm^{-1} may be attributed to the A_{1g} band of some of the spinel phase present in the sample as has already been observed in other rock-salt structures [32-34].

Additionally, Raman experiments were also performed on the stoichiometric $NiFe_2O_4$ film modifying the light polarization. Fig. 4b presents the Raman spectra with xx , xy , yx and yy indicating the polarization of the incident and scattered light, respectively. Depending on the incident and scattered configuration, changes in the relative intensity of the modes are clearly noted while the modifications in the band positions are insignificant. These findings corroborate the epitaxial character of the $NiFe_2O_4$ film, and changes with respect to those expected for the $Fd\bar{3}m$ structure are explained by the distribution of the Ni and Fe cations

in the stoichiometric structure, as commented above and reported for the NFO structure [6, 35].

In order to confirm the structural dependence on the Ni content, the environment of the different cations present in the samples as well as their oxidation states have been evaluated by XAS measurements. Figure 5a and 5b show the experimental XANES spectra at the Fe and Ni K-edge, respectively, for all samples varying the Ni/Fe proportion. For different samples, at each absorption edge, similar absorption characteristics are observed. The oxidation state of the absorbing atom in each sample can be determined from the linear relationship between the absorption edge position and the average oxidation state of atoms by using specific references [36, 37]. At the Fe K-edge (see Fig. 5a), the main absorption edge is very close to that of Fe_3O_4 reference, indicating that the oxidation state is 2.6^+ for the Fe cations of all films [36,38]. At the Ni K-edge (see Fig. 5b), the position of the main absorption edge is close to that of the NiO reference with an average oxidation state of 2^+ of the Ni cations [39, 40]. Specifically, in this case, a slight variation at the absorption edge position of samples can be noted towards lower energy values as Ni fraction increases, which may relate to a reduction of the average valence or to the environment around the Ni cations. However, the changes are minimal.

At the Fe K-edge, a pre-peak absorption edge around 7114 eV is identified for all films (inset of Fig. 5a), which is associated with the $1s \rightarrow 3d$ quadrupole transition and $1s \rightarrow 3d/4p$ dipole transition. The first one is related with octahedral coordination and has a very small intensity [41], while in a tetrahedral environment the 3d and 4p orbitals hybridize and the dipolar transition, forbidden in octahedral symmetry, is allowed and the pre-peak intensity increases [42]. In our samples, we observe a decrease of the intensity as the Ni proportion increases, which can be related to a decrease of the tetrahedral environment around the Fe cations. In addition, this pre-peak is also sensitive to the cation oxidation state [36], with a similar position for all films indicating the same valence for the Fe cations and corroborating 2.6^+ as the average oxidation state.

The modifications at whiteline at both Fe and K-edge are identified for the different films, which can be attributed to the changes in the coordination of the absorbing cations. These can be confirmed by EXAFS spectra in the Fig. 5c and 5d at the Fe and Ni K-edge, respectively. In the Fe K-edge EXAFS signal (Fig. 5c), three shells are clearly identified for all films except for that with the greatest Ni fraction. The first shell is located around 2.0 Å and is associated with the distances of Fe located in both tetrahedral and octahedral positions with oxygen atoms (Fe-O bonds). The second shell around 2.9 Å corresponds to the distance of octahedral Fe atoms to their second neighbours located at octahedral sites ($\text{Fe}_\text{O}\text{-Fe}_\text{O}/\text{Ni}_\text{O}$), and the third shell around 3.4 Å corresponds to the distance between Fe cations located at octahedral positions and atoms located at tetrahedral positions, and between Fe/Ni cations located at tetrahedral position and atoms located at octahedral ones ($\text{Fe}_\text{O,T}\text{-Fe}_\text{O,T}/\text{Ni}_\text{O,T}$ neighbours). The most significant changes of k^3 -weighted EXAFS spectra correspond to the intensity of shells, which may be attributed to the coordination of Fe cations decreasing as the Ni proportion increases. As commented above, specifically for the film with the highest amount of Ni, the disappearance of the third shell is identified. This feature can be explained by the removal of the Fe/Ni at tetrahedral positions as was noted by the pre-peak intensity in the XANES signal [43].

At the Ni K-edge, the k^3 -weighted EXAFS spectra show also three-shells. The first peak appears around 2.0 Å related to the distance with the first Ni neighbours and the oxygen atoms (Ni-O). The second coordination shell appears around 2.9 Å and is related to Ni cations and atoms located at octahedral positions (Ni-Fe_o/Ni_o neighbours). The third shell, around 3.4 Å, corresponds to Ni cations coordinated with Fe cations in tetrahedral sites. This last one reduces its intensity with the Ni fraction in the films, disappearing for the sample with the highest Ni content according to the results at the Fe K-edge.

Therefore, both XANES and EXAFS results confirm the structural transformation from spinel to disorder rock-salt structure of Ni_xFe_{3-x}O_y films where the average valence of the absorbing atoms is retained and the tetrahedral coordination disappears for the highest Ni content, in agreement with a rock-salt structure and XRD and Raman experiments.

The physical properties as resistivity and energy optical gaps show significant changes with Ni concentration in the ferrite. Fig. 6a shows the variation of electrical conductivity with the reciprocal temperature (1000/T) for the different (111) Ni_xFe_{3-x}O_y thin films. All the thin films show a semiconducting nature that can be observed by the increasing electrical conductivity with temperature. The Arrhenius plot reveals a straight line in the measured temperature region indicating that only one conduction mechanism occurs within the studied temperature range. Fig. 6b shows the electrical resistivity of the (111) Ni_xFe_{3-x}O_y thin films at room temperature as the Ni content increases. The lowest resistivity is obtained for the spinel films with $x \leq 1$, i.e. 1.5 ohm·cm, and the value increases until 940 ohm·cm for the highest Ni concentration when the films is dominated by a rock-salt structure. The resistivity value of stoichiometric film, i.e. 1.5 ohm·cm, is lower than the observed in ferrite bulk, i.e. $1 \cdot 10^3$ ohm·cm [44], however is in the wide range observed in stoichiometric NFO thin films ($1 \cdot 10^3$ to $1 \cdot 10^{-1}$ ohm·cm) depending of oxygen partial pressure and deposition method [4, 14, 22]. For the stoichiometric film, its resistivity in the low reported range resistivity values supports the incomplete oxidation of Fe atoms to 3⁺ as determined by XANES.

The observed dependence of the resistivity and activation energy with Ni concentration in the films has been shown in both, Ni_xFe_{3-x}O₄ powders [45] and films [22], which is attributed to an increasing electrical conduction as Fe increases. The analysis of the straight part provides an activation energy, E_a , that increases with the Ni content between 0.12 for $x \leq 1$ up to 0.31 eV for $x = 1.7$. This behavior with the Ni concentration has also been observed in Ni_xFe_{3-x}O₄ powders [45], however in a different temperature range, i.e. from 500 to 800 °C, giving values of E_a between 0.14 and 0.24 eV. Related to NFO films, our values are in the range of the values obtained for stoichiometric NFO films at room temperature, i.e. 0.23 eV [14].

The electrical properties of spinel oxides are closely related to the cationic distributions on tetrahedral and octahedral sites and its oxidation states. In our case, we have to consider to different cationic compositional range to explain the result. For magnetite, it is well established that the electrical conductivity originates from the electron hopping between the mixed-valence Fe²⁺ and Fe³⁺ ions at octahedral sites i.e. $\text{Fe}^{3+} + e^- \leftrightarrow \text{Fe}^{2+}$ [16, 22]. When Ni is incorporated in the spinel structure of magnetite, mainly at octahedral sites, induce the

decrease of Fe^{2+} - Fe^{3+} pairs at octahedral sites, resulting in the increase of the electrical resistivity. This thermally activated electron hopping conduction mechanism can explain our result for stoichiometric and close to stoichiometric NFO thin films, i.e. $0.7 \leq x \leq 1.2$ in $\text{Ni}_x\text{Fe}_{3-x}\text{O}_y$. For the highest Ni content film, the $\text{Fe}^{2.6+}$ remaining cations are mainly at octahedral sites, as we have determined by XANES and EXAFS, so the reduced resistivity expected by a reduced number of Fe cations could be compensated by its localization at octahedral sites. Then, in order to explain the strong increasing resistivity up to three magnitude orders, we have to consider the structural change to rock-salt structure.

NiO is a Mott-Hubbard insulator at room temperature. The substitution of Ni by Fe in the rock-salt structure generates disorder, since Fe is randomly localized over the host lattice, defects and Ni vacancies that can modify the insulating nature of NiO ($\rho \sim 10^{13} \Omega \cdot \text{cm}$) by changing it to semiconductor behavior [46]. Additionally, Fe dopants in NiO are generally used to induce ferromagnetism but also to change its optical properties [46, 47]. The phase diagram of the Ni-Fe-O systems reports a stable rock-salt structure up to iron concentration of 40% depending of temperature and oxygen partial pressure [48]. In this scenario, we can understand the electric properties of the film with $x=1.7$, i.e. $\sim 43\%$ of Fe cations, in terms of Fe-doped NiO with a disorder rock-salt structure plus probably secondary contributions of disorder spinel $(\text{Fe},\text{Ni})_3\text{O}_4$ as suggested by the Ni-Fe-O phase diagram [46], and by the presence of its A_{1g} vibrational mode observed in the Raman spectrum.

Fig. 7a shows the transmittance spectra of $\text{Ni}_{0.7}\text{Fe}_{2.3}\text{O}_y$ and $\text{Ni}_{1.7}\text{Fe}_{1.3}\text{O}_y$ thin film. An increase of transmittance, with increasing Ni content in the films over the whole range analyzed, is clearly observed. The reflectance spectra (Fig. 7b) and the film absorption coefficient (not shown) are obtained following the strategy of Cesaria *et al.* for thin films deposited on thick transparent or semi-transparent substrates [49]:

$$\alpha_Y(\lambda) = \frac{1}{d_Y} \ln \frac{1-R_Y(\lambda)}{T_Y(\lambda)} \quad (1)$$

where Y represent the substrate or the total stack (film+substrate), d the thickness, α the absorption coefficient and T and R the transmittance and reflectance respectively. The absorption coefficient of the film is calculated from:

$$\alpha_{film}(\lambda) = \left(\frac{d_{substrate}}{d_{film}} \right) (\alpha_{total}(\lambda) - \alpha_{substrate}(\lambda)) \quad (2)$$

while the reflectance is obtained from the inversion of equation (1).

We have observed similar reflectance maximum values, $\approx 30\%$, for all the films and a reduction of the absorption coefficient as the Ni content increases. The relationship between the absorption coefficient and the photon energy ($h\nu$) can be used to determine the optical energy gap applying the Tauc's equation:

$$(\alpha h\nu)^2 = A(h\nu - E_g)^n \quad (3)$$

in which A is a constant, E_g is the band gap energy and n is a constant, taking values of $\frac{1}{2}$ and 2 for direct and indirect allowed transitions, respectively.

From Fig. 7c, the existence of two direct band gaps for $\text{Ni}_x\text{Fe}_{3-x}\text{O}_y$ thin films with $x \leq 1.2$ is observed, while the film with the highest Ni content, i.e. $\text{Ni}_{1.7}\text{Fe}_{1.3}\text{O}_y$, only shows one direct band gap at 3.22 eV. Direct and indirect band gaps of films as a function of Ni content are represented in Fig. 7d. The presence of two direct band gaps is related to the two types of interband transitions that take place in spinel ferrites with inverse configuration [50]. The energy gap assigned to majority channels ranges between 2.65 and 2.75 eV and the one assigned to minority channels ranges between 2.26 and 2.29 eV, in good agreement with first-principle calculations and experimental results [50, 51]. The top of the valence band is formed by octahedral Ni d states for both majority and minority channels and the bottom of the conduction band is formed by octahedral Fe d states in the minority channel and tetrahedral Fe d states in the majority channel [50]. In the case of the highest Ni content film, the increasing amount of Fe atoms at octahedral sites respect to tetrahedral ones induces the presence of an only clearly visible energy gap. In addition, and in good agreement with experimental and theoretical calculation, we have found that the $\text{Ni}_x\text{Fe}_{3-x}\text{O}_y$ films are indirect gap materials with an almost linear increasing indirect energy gap with Ni content from 1.42 to 1.62 eV assigned to phonon-assisted minority channels [51].

Conclusions

We have demonstrated that ion beam sputtering is a suitable technique to grow epitaxial (111) nickel ferrite thin films with tunable structural, electrical and optical properties, tailoring the cationic composition: Ni content from 0.7 to 1.7 in $\text{Ni}_x\text{Fe}_{3-x}\text{O}_y$. Epitaxial spinel structural films show an out-of-plane lattice parameter dependent on the Ni content. In addition, an ordered spinel-disordered rock-salt transition is identified as the Ni content exceeds the stoichiometric value, i.e. $x=1$. The observed cationic environment changes as well as the electrical and optical properties of the films, supporting the structural transition. Specifically, an increasing resistivity up to three orders of magnitude is identified with the Ni content. Besides, an increase of energy of the two direct optical band gaps characteristic of the spinel structural films and indirect optical gap is obtained, detecting only one direct band gap for the film with the rock-salt structure.

Acknowledgments

This investigation has been funded by the Comunidad de Madrid through the NANOMAGCOSTCM-P2018/NMT4321 project and by the MINECO of Spain through the RTI2018-095303-A-C52 and RTI2018-095303-A-C51 projects. We acknowledge the support from CMAM for the beam time proposals with codes P00736 and P00684. Part of these experiments were performed at the CLÆSS-BL22 beamline at ALBA Synchrotron (grant number 2020094658). Giulio Gorni is especially grateful for his support during the XAS measurements. A.S. acknowledges the financial support from the Comunidad de Madrid for an “Atracción de Talento Investigador” contract (No. 2017-t2/IND5395). We

also acknowledge the support of Miguel Manso Silván for the optical characterization of the films.

References

- [1] W.A.M. Braders, Handbook of Magnetic Materials, vol.8, K. H. J. Buschow, Ed. Amsterdam, The Netherlands: Elsevier, 1995, pp 189-324.
- [2] C.Himcinschi, I. Vrejoiu, G. Salvan, M. Fronk, A. Talkenberger, D. R. T. Zahn, D. Rafaja, J. Kortus, Optical and magneto-optical study of nickel and cobalt ferrite epitaxial thin films and submicron structures, Journal of Applied Physics, 113, (2013) 084101. <https://doi.org/10.1063/1.4792749>.
- [3] E.P. Wohlfarth and K.H.J. Buschow, Ferromagnetic Materials: A Hand book on the Properties of Magnetically Ordered Substances, ed. North-Holland, Amsterdam, 1980.
- [4] U. Lüders, A. Barthélémy, M. Bibes, K. Bouzehouane, S. Fusil, E. Jacquet, J.P. Contour, J.P. Bobo, J. Fontcuberta and A. Fert, NiFe₂O₄: A Versatile Spinel Material Brings New Opportunities for Spintronics, Adv. Mater. 18 (2006) 1733–1736. <https://doi.org/10.1002/adma.200500972>.
- [5] D. Carta, M. F. Casula, A. Falqui, D. Loche, G. Mountjoy, C. Sangregorio and A. Corrias, A Structural and Magnetic Investigation of the Inversion Degree in Ferrite Nanocrystals MFe₂O₄ (M) Mn, Co, Ni), J. Phys. Chem. C 113 (2009) 8606–8615. <https://doi.org/10.1021/jp901077c>.
- [6] M.N. Iliev, D. Mazumdar, J.X. Ma, A. Gupta, F. Rigato and J. Fontcuberta, Monitoring B-site ordering and strain relaxation in NiFe₂O₄ epitaxial films by polarized Raman spectroscopy, Physical Review B 83 (2011) 014108. <https://doi.org/10.1103/PhysRevB.83.014108>.
- [7] G. Dixit, J.P. Singh, R.C. Srivastava, H.M. Agrawal, R.J. Chaudhary, Structural, magnetic and optical studies of nickel ferrite thin films, Adv. Mat. Lett. 3(1) (2012) 21-28. <http://DOI:10.5185/amlett.2011.6280>.
- [8] M. Hoppe, M. Gorgoi, C.M. Scheneider and M. Müller, Wide-Range Structural and Chemical Stability of the Magnetic Oxide NiFe₂O₄ Grown by O₂- Assisted Pulsed Laser deposition, IEEE Transactions on Magnetism 50(11) (2014) 25206204. <http://10.1109/TMAG.2014.2322378>.
- [9] S. Anjum, G. H. Jaffari, A. K Rumaiz, M S. Rafique¹ and S. I. Shah², *Role of vacancies in transport and magnetic properties of nickel ferrite thin films*, J. Phys. D: Appl. Phys. 43 (2010) 265001. doi:10.1088/0022-3727/43/26/265001.
- [10] J.E. Bratvold, H. H. Sønsteby, O. Nilsen and Helmer Fjellvåg, Control of growth orientation in as-deposited epitaxial iron-rich nickel ferrite spinel, J. Vac. Sci. Technol. A 37(2) (2019) 021502. <https://doi.org/10.1116/1.5082012>.
- [11] N. Pachauri, B. Khodadadi, A. V. Singh, J. B. Mohammadi, R.L.Martens, P. R. LeClair, C. Mewesm T. Mewes and A. Gupta, A comprehensive study of ferromagnetic resonance and structural properties of iron-rich nickel ferrite (Ni_xFe_{3-x}O₄) films grown by chemical vapor deposition, Journal of Magnetism and Magnetic Materials 417 (2016) 137–142. <https://doi.org/10.1016/j.jmmm.2016.05.045>.

- [12] A. Mandziak, J. de la Figuera, S. Ruiz-Gómez, G.D. Soria, L. Pérez, P. Prieto, A. Quesada, M. Foerster and L. Aballe. Structure and magnetism of ultrathin nickel-iron oxides grown on Ru(0001) by high-temperature oxygen-assisted molecular beam epitaxy, *Scientific Reports* 8 (2018)17980. DOI:10.1038/s41598-018-36356-6.
- [13] DMeier, T. Kuschel, L. Shen, A. Gupta, T. Kikkawa, K. Uchida, E. Saitoh, J.-M. Schmalhorst, and G. Reiss, Thermally driven spin and charge currents in thin NiFe₂O₄/Pt films, *Phys. Rev. B.* 87 (2013) 054421. 10.1103/PhysRevB.87.054421.
- [14] C. Klewe, M. Meinert, A. Boehnke, K. Kuepper, E. Arenholz, A. Gupta, J.-M. Schmalhorst, T. Kuschel and G. Reiss, Physical characteristics and cation distribution of NiFe₂O₄ thin films with high resistivity prepared by reactive co-sputtering, *Journal of Applied Physics* 115 (2014) 123903. <https://doi.org/10.1063/1.4869400>.
- [15] J. Morishita, T. Niizeki, K. Z. Suzuki, H. Yanagihara and E. Kita, Magnetic and Electrical Properties of Epitaxial NiFe₂O₄ (001) Films Fabricated by Reactive Sputtering, *IEEE Transactions on Magnetics*, vol. 50(11) (2014) 2303904. DOI:10.1109/TMAG.2014.2326664.
- [16] C. Solís, S. Somacescu, E. Palafox, M. Balaguer and J. M. Serra, Particular Transport Properties of NiFe₂O₄ Thin Films at High Temperatures, *J. Phys. Chem. C* 118,42 (2014) 24266–24273. <https://doi.org/10.1021/jp506938k>.
- [17] J. Shan, P. Bougiatioti, L. Liang, G. Reiss, T. Kuschel and B.J. van Wees, Nonlocal magnon spin transport in NiFe₂O₄ thin films, *Appl. Phys. Lett.* 110 (2017) 132406. <https://doi.org/10.1063/1.4979408>.
- [18] Y. Liu, Z. Mei, Y. Guo, P. Zhou, Y. Qi, K. Liang, Z. Ma, Z. Xia, A. Adhikary, C. Dong, N. Sun, G. Shirivasan and T. Zhang, Evidence for strain control of magnetic anisotropy in epitaxial nickel ferrite thin films grown on strontium titanate substrates, *Materials Research Bulletin* 138 (2021) 111214. <https://doi.org/10.1016/j.materresbull.2021.111214>.
- [19] S. Seifikar, B. Calandro, E. Deeb, E. Sachet, J. Yang, J.. Maria, N. Bassiri-Gharb, J. Schwartz, Structural and magnetic properties of biaxially textured NiFe₂O₄ thin films grown on c-plane sapphire, *Journal of Applied Physics* 112 (2012) 123910. <https://doi.org/10.1063/1.4770366>.
- [20] S. Seifikar, B. Calandro, G. Rasic, E. Deeb, J. Yang, N. Bassiri-Gharb and J. Schwartz, Optimized Growth of Heteroepitaxial (111) NiFe₂O₄ Thin Films on (0001) Sapphire with Two In-Plane Variants via Chemical Solution Deposition, *J. Am. Ceram. Soc.*, 96 (10) (2013)3050–3053. <https://doi.org/10.1111/jace.12520>.
- [21] K. Kim, T.Y. Koh, J. Park and J.Y. Park Effects of Octahedral Ni²⁺ on Structural and Transport Properties of Ni_xFe_{3-x}O₄ Thin Films, *Journal of Magnetism* 22(3) (2017) 360-363. DOI:10.4283/JMAG.2017.22.3.360.
- [22] C Jin, Q Zhang, W B Mi, E Y Jiang and H L Bai, Tunable magnetic and electrical properties of polycrystalline and epitaxial Ni_xFe_{3-x}O₄ thin films prepared by reactive co-sputtering, *Phys. D: Appl. Phys.* 43 (2010) 385001.doi:10.1088/0022-3727/43/38/385001.

- [23] J. Rodewald, J. Thien, T. Pohlmann, M. Hoppe, F. Bertram, K. Kuepper, and J. Wollschläger, Real-time monitoring the growth of strained off-stoichiometric ultrathin films on MgO(001), Appl. Phys. Lett. 117 (2020) 011601. <https://doi.org/10.1063/5.0013925>.
- [24] A. Redondo-Cubero M. J. G. Borge1, N. Gordillo, P. C. Gutiérrez,J. Olivares, R. Pérez Casero, M. D. Ynsa1, Current status and future developments of the ion beam facility at the centre of micro-analysis of materials in Madrid, Eur. Phys. J. Plus (2021) 136-175. <https://doi.org/10.1140/epjp/s13360-021-01085-9>.
- [25] M. Mayer, Simnra: A simulation program for the analysis of nra, rbs and erda, AIP Conf. Proc., 475 (1) (1999), pp. 541-544, 10.1063/1.59188
- [26] L. Simonelli, C. Marini, W. Olszewski, M. Ávila Pérez, N. Ramanan, G. Guilera, et al., CLÆSS: The hard X-ray absorption beamline of the ALBA CELLS synchrotron, Cogent Phys. 3 (2016). doi:10.1080/23311940.2016.1231987.
- [27] H. Fjellvag, F. Gronvold, S. Stolen, B.C. Hauback, On the crystallographic and magnetic structures of nearly stoichiometric iron monoxide. Journal of Solid State Chemistry 124 (1996) 52-57 (1996).DOI:10.1006/jssc.1996.0206.
- [28] A. Leineweber, H. Jacobs, S. Hull, Ordering of Nitrogen in Nickel Nitride Ni₃N Determined by Neutron Diffraction, Inorganic Chemistry 40 (2001) 5818-5822.. <https://doi.org/10.1021/ic0104860>.
- [29] K. Aleksandar, A. Bratislav, V.V. Milica, C. Philippe, J. Cedimir, B. Natasa, K.Volker, L. Matteo, Temperature-induced structure and microstructure evolution of nanostructured Ni_{0.9}Zn_{0.1}O, Journal of Applied Crystallography 43(4) (2010) 699-709. DOI:10.1107/S0021889810019163.
- [30] H. Sharona, B. Loukya, U. Bhat, R. Sahu, B. Vishal, P. Silwal, A. Gupta, and R. Datta, Coexisting nanoscale inverse spinel and rock salt crystallographic phases in NiCo₂O₄ epitaxial thin films grown by pulsed laser deposition, Journal of Applied Physics 122, 225301 (2017). <https://doi.org/10.1063/1.4998776>.
- [31] A.Ahlawat and V.G. Sathe, Raman study of NiFe₂O₄ nanoparticles, bulk and films: effect of laser power, J. Raman Spectrosc. 42 (2011) 1087. <https://doi.org/10.1002/jrs.2791>.
- [32] E. Aytan, B. Debnath, F. Kargar, Y. Barlas, M. M. Lacerda, J. X. Li, R. K. Lake, J. Shi, and A. A. Balandin, Spin-phonon coupling in antiferromagnetic nickel oxide, Appl. Phys. Lett. 11, 252402 (2017). <https://doi.org/10.1063/1.5009598>.
- [33] B. Rivas-Murias,V. Salgueiriño, Thermodynamic CoO–Co₃O₄ crossover using Raman spectroscopy in magnetic octahedron-shaped nanocrystals, 48 (2017) 837-841. <https://doi.org/10.1002/jrs.5129>
- [34] A. Kremenovic, B. Antic, M. Vucinic-Vasic, P. Colomban, C. Jovalekic, N. Bibic, V. Kahlenberg, M. Leoni, Temperature-induced structure and microstructure evolution of nanostructured Ni_{0.9}Zn_{0.1}O, J. Appl. Cryst. 43 (2010) 699-709. <https://doi.org/10.1107/S0021889810019163>

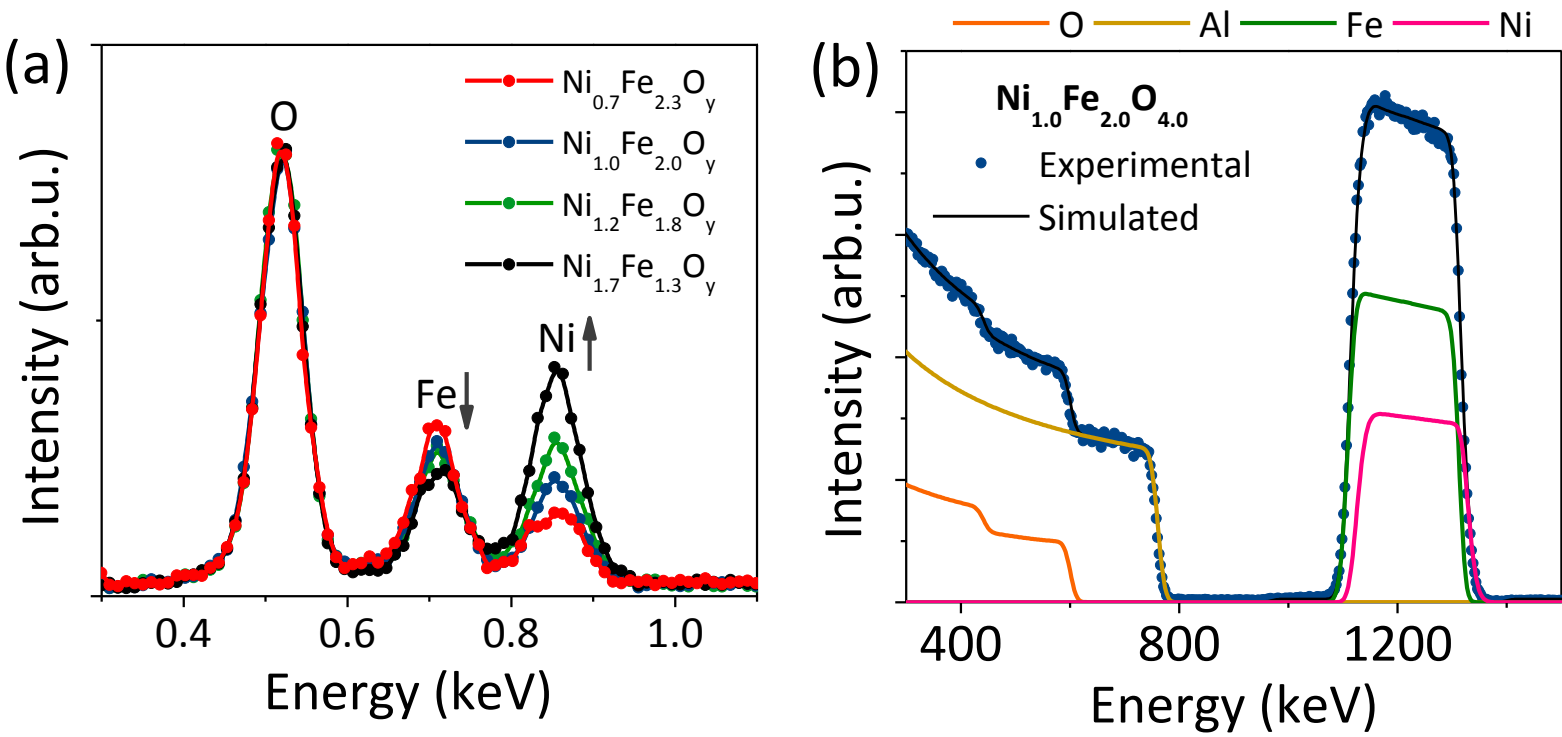
- [35] N.Li, Y-H.A. Wang, M. N. Iliev, T. M. Klein, A. Gupta, Growth of Atomically Smooth Epitaxial Nickel Ferrite Films by Direct Liquid Injection CVD, *Chem. Vap. Deposition* 17 (2011) 261–269. <https://doi.org/10.1002/cvde.201106930>.
- [36] J. Rubio-Zuazo, A. Chainani, M. Taguchi, D. Malterre, A. Serrano, G.R. Castro, Electronic structure of FeO, γ -Fe₂O₃ and Fe₃O₄ epitaxial films using high-energy spectroscopies, *Phys. Rev. B* 97,1–9 (2018).
- [37] M. Abuin, A. Serrano, J. Chaboy, M.A. García, N. Carmona, XAS study of Mn, Fe and Cu as indicators of historical glass decay, *J. Anal. At. Spectrom.*, 28, 1118 (2013).
- [38] D. Malferrari, E. Castellini, F. Bernini, A. Serrano Rubio, G.R. Castro, C.I. Sainz-Díaz, M. Caleffi, M.F. Brigatti, M. Borsaria, Chemical trapping of gaseous H₂S at high and low partial pressures by an iron complex immobilized inside the montmorillonite interlayer, *Microporous and Mesoporous Materials*, 265, 15, 8-17 (2018).
- [39] A. S. Albuquerque, J. D. Ardisson, and W. A. A. Macedo, Nanosized powders of NiZn ferrite: Synthesis, structure, and magnetism, *J. Appl. Phys.* 87, 4352 (2000).
- [40] Thanit Tangcharoen, Wantana Klysubun, Chanapa Kongmark, and Wisanu Pecharapa, Synchrotron X-ray absorption spectroscopy and magnetic characteristics studies of metal ferrites (metal^{1/4}Ni, Mn, Cu) synthesized by sol–gel auto-combustion method, *Phys. Status Solidi A* 211, No. 8, 1903–1911 (2014).
- [41] M. Fracchia, M. Manzoli, U. Anselmi-Tamburini, P. Ghigna, A new eight-cation inverse high entropy spinel with large configurational entropy in both tetrahedral and octahedral sites: Synthesis and cation distribution by X-ray absorption spectroscopy, *Scr. Mater.* 188 (2020) 26–31.
- [42] M. Rivero, A. Serrano, J.A. Rodríguez-Velamazán, A. Muñoz-Bonilla, J. Sánchez-Marcos, Understanding the structural and magnetic evolution of superparamagnetic Zn ferrites nanoparticles synthesized by an easy electrochemical process, *Journal of Alloys and Compounds* 881 (2021) 160585.
- [43] D. Zhou, S. Permien, J. Rana, M. Krengel, F. Sun, G. Schumacher, W. Bensch, J. Banhart, Investigation of electronic and local structural changes during lithium uptake and release of nanocrystalline NiFe₂O₄ by X-ray absorption spectroscopy, *Journal of Power Sources* 342 (2017) 56-63.
- [44] V. A. M. Brabers, in *Handbook of Magnetic Materials*, Vol. 8 (Ed:K. H. J. Buschow), North-Holland, Amsterdam, The Netherlands 1982, Ch. 3.
- [45] D. A. Chesson and J. H. Zhuz, Effect of Off-Stoichiometry on Electrical Conductivity in Ni-Fe and Mn-Co Spinel Systems, *Journal of The Electrochemical Society*, 167 (2020)124515. <https://doi.org/10.1149/1945-7111/abae3a>.
- [46] Y-H Lin, J. Wang, J. Cai, M. Ying, R. Zhao, M. Li, C.W. Nan, Ferromagnetism and electrical transport in Fe-doped NiO, *Phys. Rev. B* 73 (2006) 193308. <https://doi.org/10.1103/PhysRevB.73.193308>.
- [47] J.E. Petersen, F. Twagirayezu, L.M. Scolfaro, P. D. Borges, W.J. Geerts, Electronic and optical properties of antiferromagnetic iron doped NiO – A first principles study, *AIP Advances* 7 (2017) 055711. <https://doi.org/10.1063/1.4975493>

- [48] V. Raghavan, Fe-Ni-O (Iron-Nickel-Oxygen), JPEDAV (2010) 3 (201) 369–371. <https://doi.org/10.1007/s11669-010-9714-8>.
- [49] M. Cesaria, A.R. Caricato and M. Martino, Realistic reflectance spectrum of thin films covering a transparent optically thick substrate, Appl. Phys. Lett. 105 (2014) 031105. <https://doi.org/10.1063/1.4890675>.
- [50] K. Dileep, B. Loukya, N. Pachauri, A. Gupta and R. Datta, Probing optical band gaps at the nanoscale NiFe₂O₄ and CoFe₂O₄ epitaxial films by high resolution electron energy loss spectroscopy, Journal of Applied Physics 116 (2014) 103505. <https://doi.org/10.1063/1.4895059>.
- [51] Q.C. Sun, H. Sims, D. Mazumdar, J. X. Ma, B. S. Holinsworth, K. R. O’Neal, G. Kim, W. H. Butler, A. Gupta and J. L. Musfeldt, Optical band gap hierarchy in a magnetic oxide: Electronic structure of NiFe₂O₄, Phys. Rev. B 86 (2012) 205106. <https://doi.org/10.1103/PhysRevB.86.205106>.

Table 1. Thin film denotation according to the Ni content. Ni content, x in $\text{Ni}_x\text{Fe}_{3-x}\text{O}_y$, determined by EDS and RBS, as well as the average values. The thickness determined by RBS of four nickel ferrite thin films are also included.

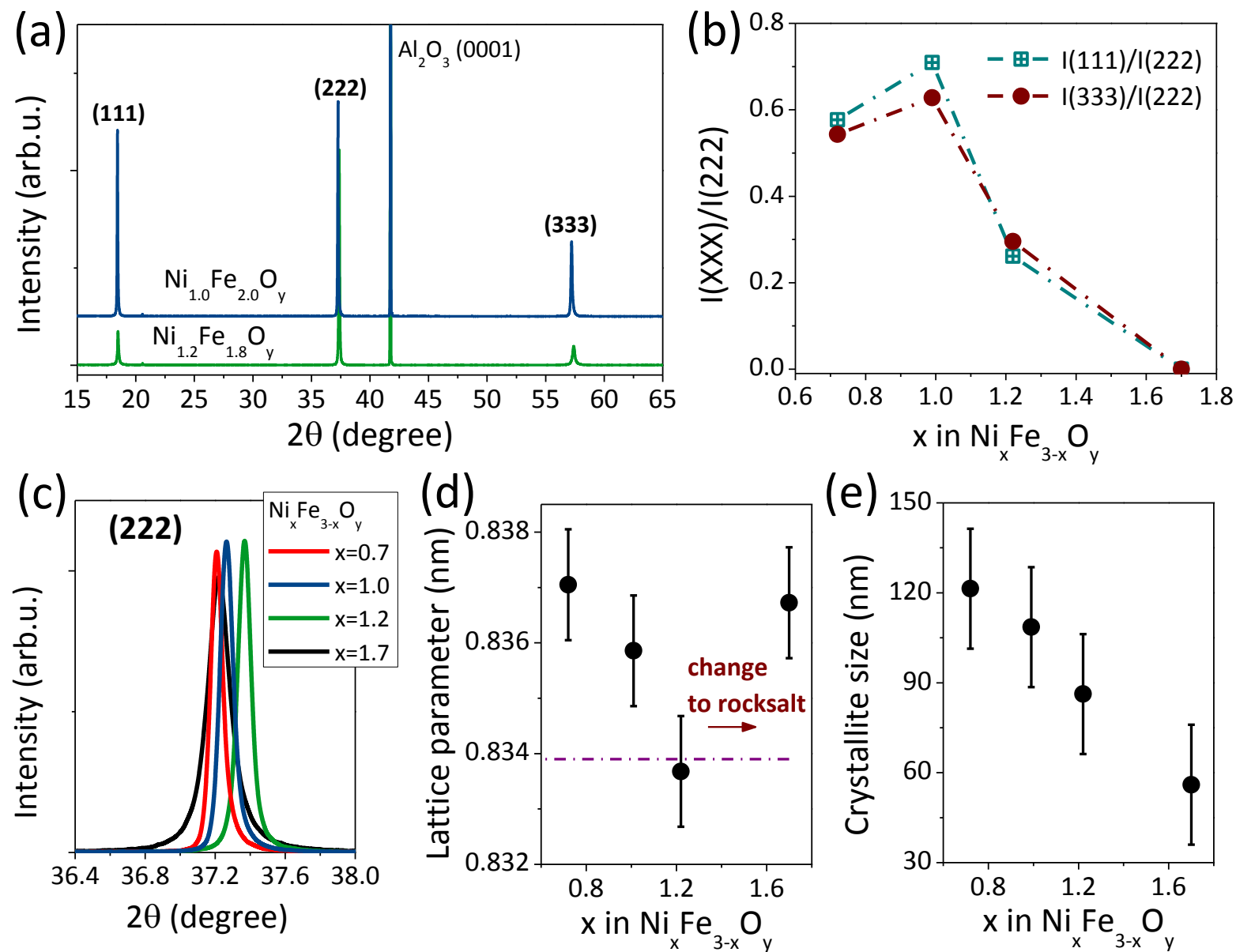
Sample	x (EDS)	x (RBS)	x	Thickness (nm)
$\text{Ni}_{0.7}\text{Fe}_{2.3}\text{O}_y$	0.68	0.80	0.74	220
$\text{Ni}_{1.0}\text{Fe}_{2.0}\text{O}_y$	0.99	1.04	1.01	214
$\text{Ni}_{1.2}\text{Fe}_{1.8}\text{O}_y$	1.28	1.20	1.24	204
$\text{Ni}_{1.7}\text{Fe}_{1.3}\text{O}_y$	1.64	1.68	1.66	212

Fig.1



Figure

Fig.2



Figure

Fig.3

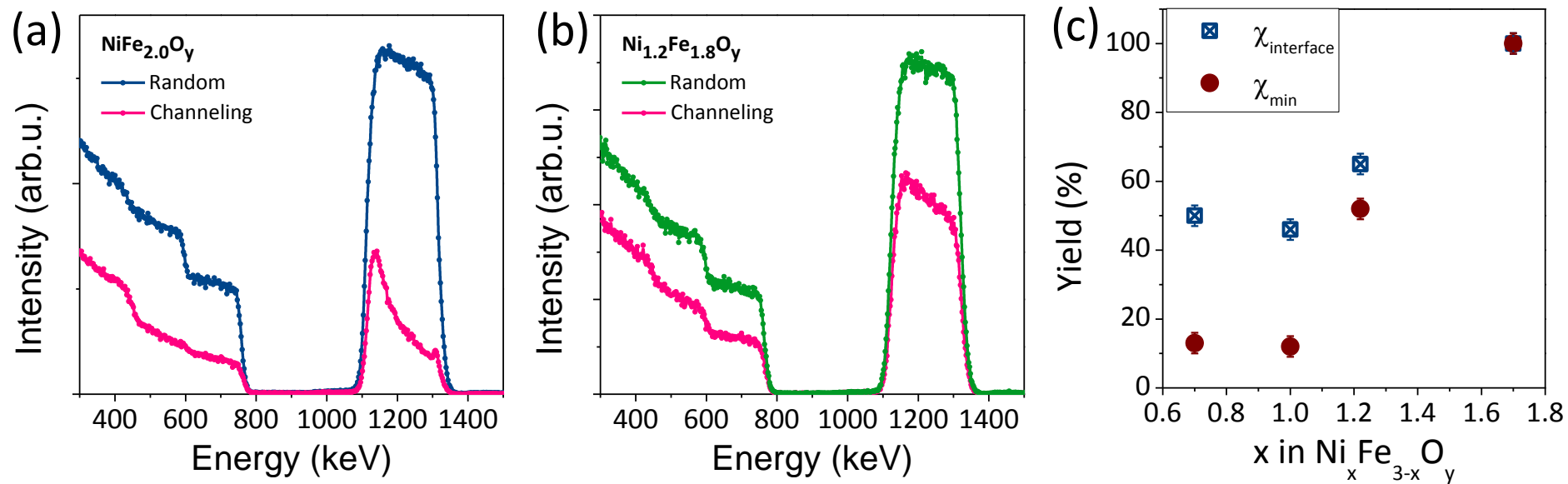


Fig.4

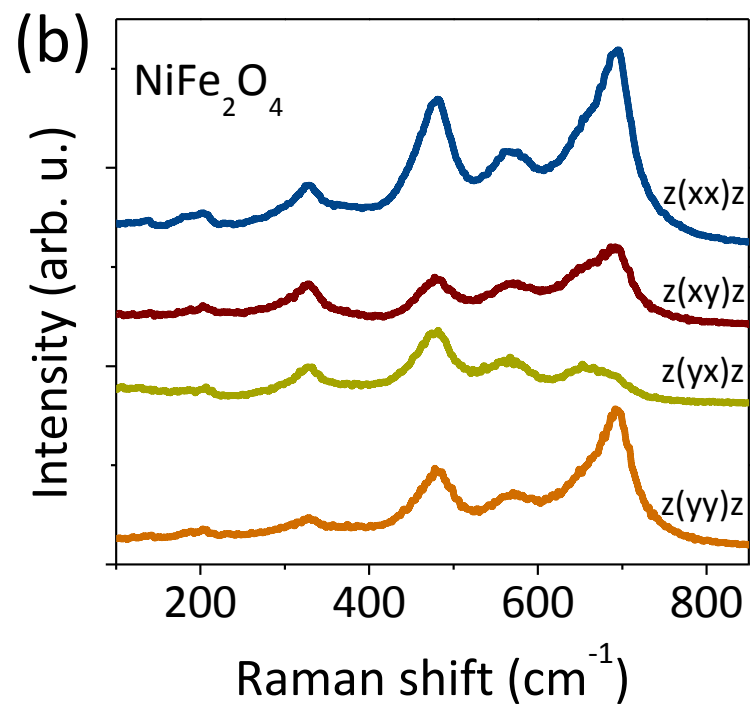
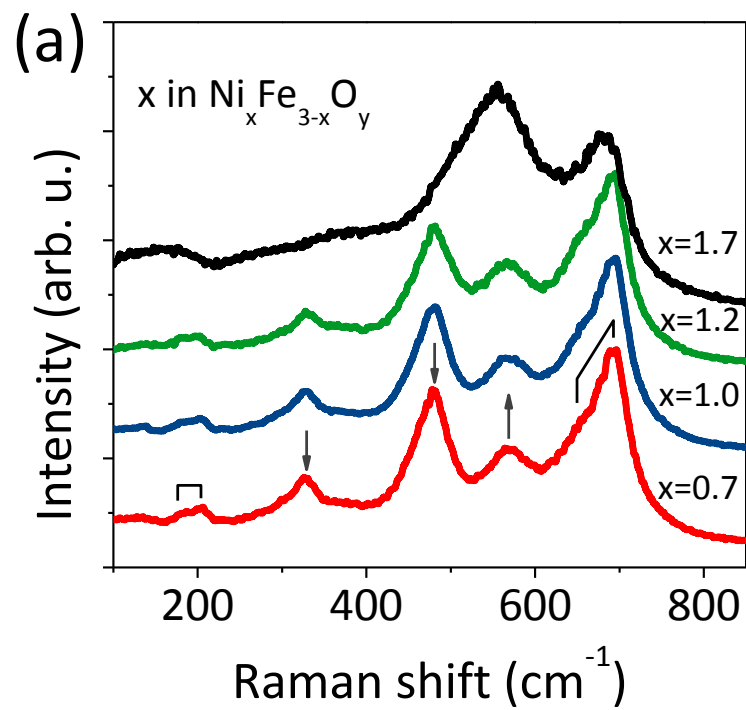


Fig. 5

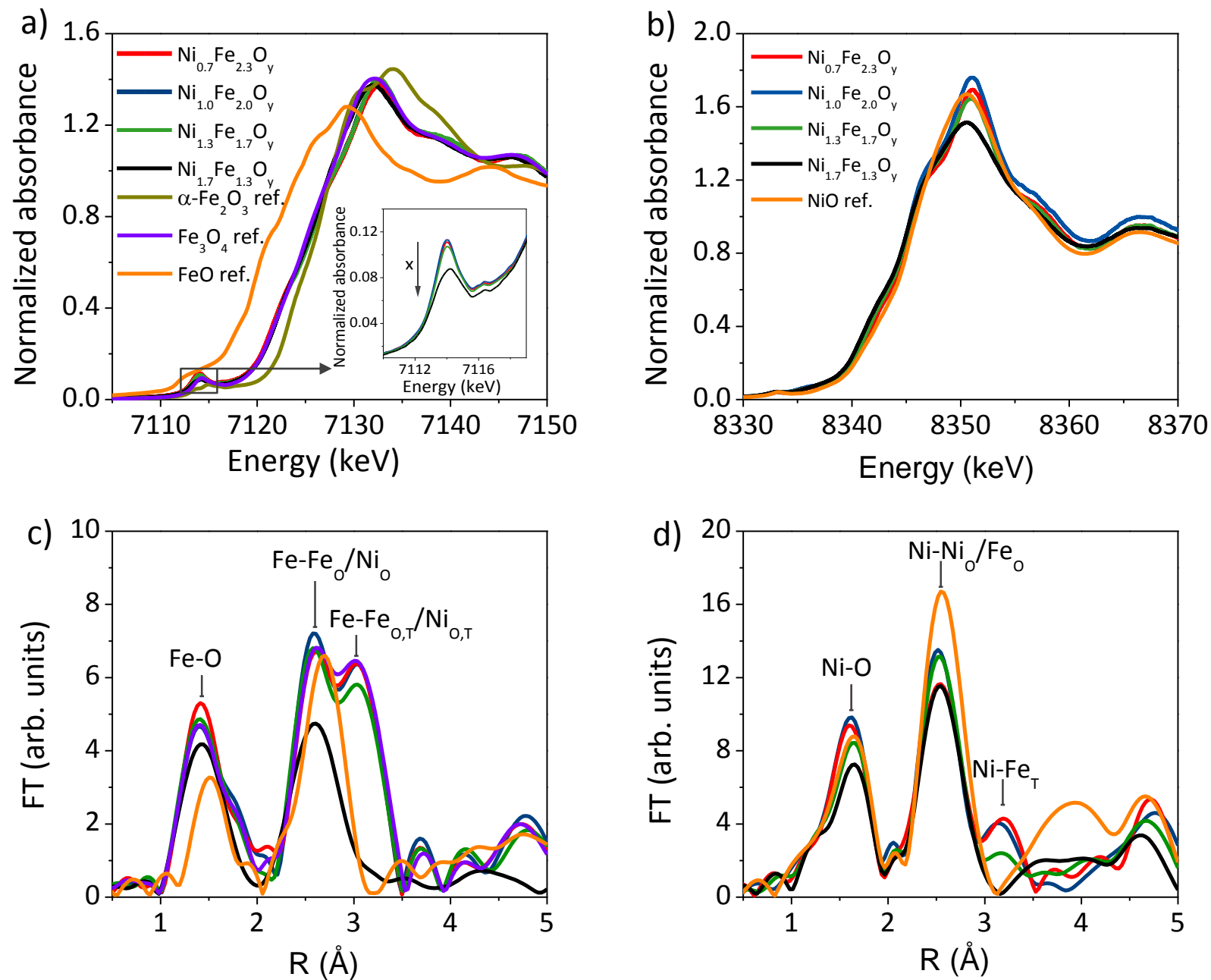
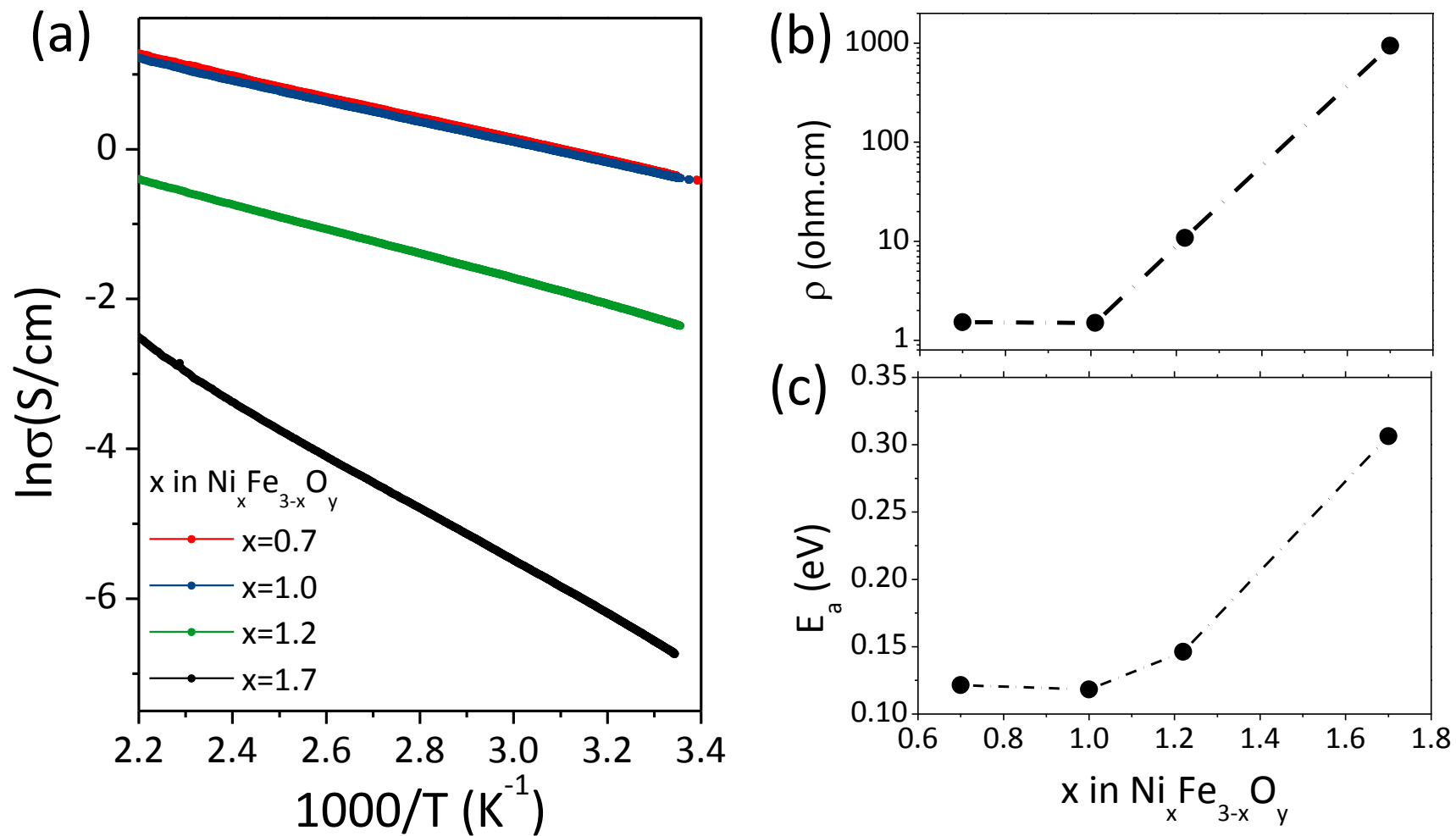


Fig.6



Figure

Fig.7

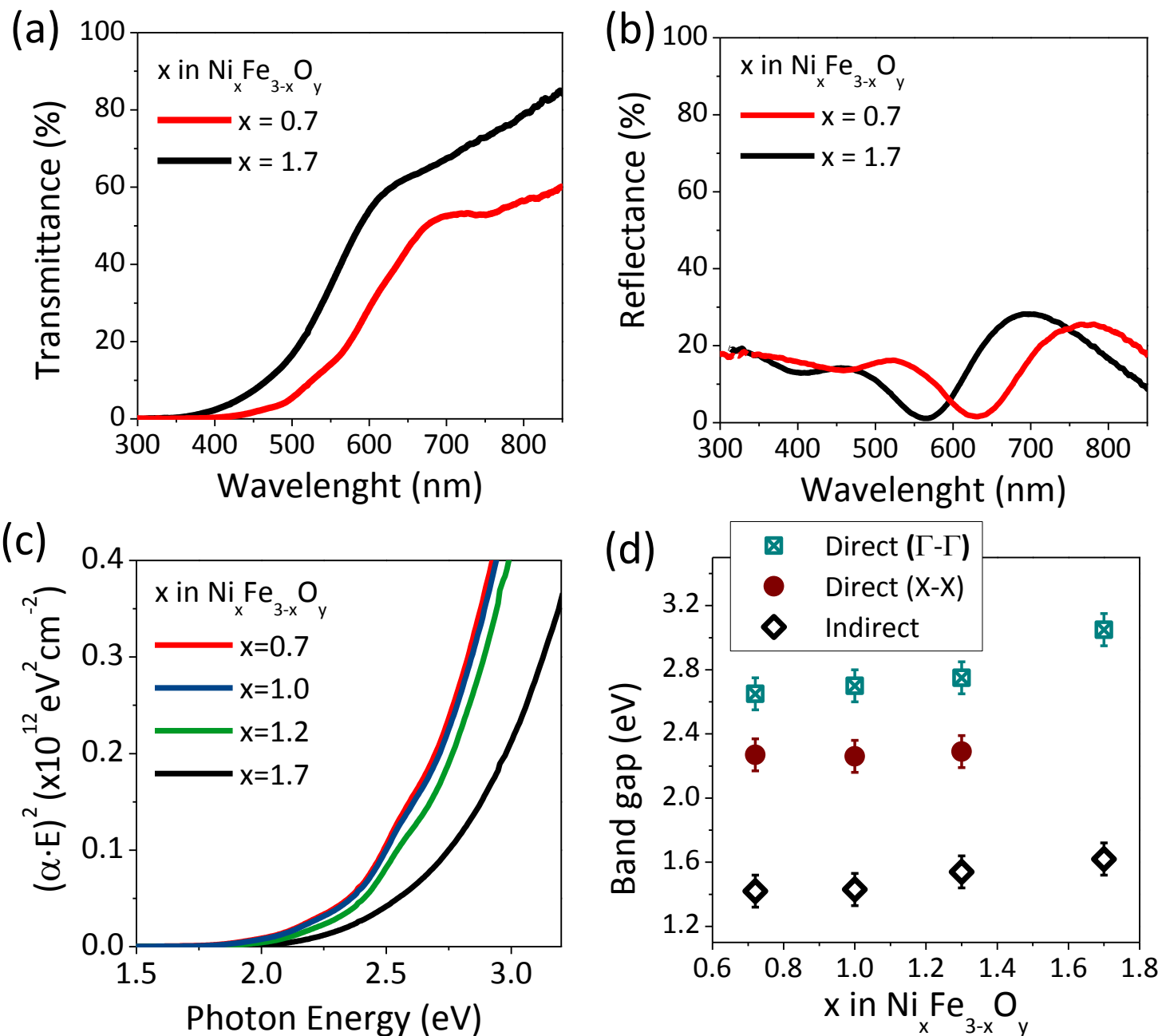


Figure Captions

Fig.1 a) EDS spectra of the $\text{Ni}_x\text{Fe}_{3-x}\text{O}_y$ thin films in which the peaks related to different elements present in the films are identified. b) Random RBS spectra of $\text{Ni}_{1.0}\text{Fe}_{2.0}\text{O}_y$ obtained with $^4\text{He}^+$ ions at 1.8 MeV and its simulation with SIMNRA program.

Fig.2 a) XRD diffraction pattern of $\text{Ni}_x\text{Fe}_{3-x}\text{O}_y$ thin films with $x = 1.0$ and $x = 1.2$ grown on Al_2O_3 (0001) substrates. b) Diffraction peak (XXX) intensity ratio respect to the (222) for $\text{Ni}_x\text{Fe}_{3-x}\text{O}_y$ thin films varying the x content. c) XRD diffraction pattern of $\text{Ni}_x\text{Fe}_{3-x}\text{O}_y$ thin films with $x = 0.7, 1.0, 1.2$ and 1.7 in the (111) rock-salt or (222) spinel 2θ range. d) Lattice parameter and e) crystalline size as a function of x in of $\text{Ni}_x\text{Fe}_{3-x}\text{O}_y$ thin films.

Fig.3 Random and (001)-aligned RBS spectra of a) $\text{Ni}_{1.0}\text{Fe}_{2.0}\text{O}_y$ and b) $\text{Ni}_{1.2}\text{Fe}_{1.8}\text{O}_y$ thin films obtained with $^4\text{He}^+$ ions at 1.8 MeV. c) Minimum yield relative to random spectra as a function of Ni content, i.e. x in $\text{Ni}_x\text{Fe}_{3-x}\text{O}_y$ at both, surface and interface.

Fig.4 a) Raman spectra of the (111) $\text{Ni}_x\text{Fe}_{3-x}\text{O}_y$ thin films with $x = 0.7, 1.0, 1.2$ and 1.7 , pointing out the shoulder-like structure of Raman bands and the trend of modes with the x content. b) Polarized Raman spectra of stoichiometric (111) NiFe_2O_4 thin film in xx, xy, yx and yy configuration.

Fig.5 XANES spectra of films at the (a) Fe and (b) Ni K-edge absorption edge. Inset of figure (a) shows the pre-edge absorption peak at the Fe K-edge. Results for reference standard compounds (FeO , $\alpha\text{-Fe}_2\text{O}_3$, Fe_3O_4 and NiO) are displayed for comparison. k^3 -weighted EXAFS spectra of films at the (c) Fe and (d) Ni K-edge. Specific shells at both absorption edge are marked.

Fig.6 a) Arrhenius of the conductivity for (111) $\text{Ni}_x\text{Fe}_{3-x}\text{O}_y$ thin films with $x = 0.7, 1.0, 1.2$ and 1.7 . b) Resistivity and c) activation energy as a function of Ni content, i.e. x in of $\text{Ni}_x\text{Fe}_{3-x}\text{O}_y$ thin films.

Fig.7 a) UV-visible transmission spectra and b) reflectance spectra of (111) $\text{Ni}_x\text{Fe}_{3-x}\text{O}_y$ thin films with $x = 0.7$ and 1.7 . c) $(\alpha h\nu)^2$ Tauc's plots and d) direct and indirect energy band gap as a function of Ni content, i.e. x in of (111) $\text{Ni}_x\text{Fe}_{3-x}\text{O}_y$ thin films, with $x = 0.7, 1.0, 1.2$ and 1.7 .